UNIVERSITY *of York*

This is a repository copy of *Photovoltaic module efficiency evaluation:The case of Iraq*.

White Rose Research Online URL for this paper:
https://eprints.whiterose.ac.uk/id/eprint/227543/

Version: Published Version

Article:

Photovoltaic module efficiency evaluation: The case of Iraq

Moustafa Al-Damook [a,d,*], **Kaleid Waleed Abid** [a], **Asim Mumtaz** [b],
Darron Dixon-Hardy [c], **Peter J. Heggs** [c], **Mansour Al Qubeissi** [d,*]

[a] *Renewable Energy Research Centre, University of Anbar, Al Anbar Province, Iraq*
[b] *Department of Physics, Stephenson Institute for Renewable Energy, University of Liverpool, Chadwick Building, Peach St, Liverpool L69 7ZF, United Kingdom*
[c] *School of Chemical and Process Engineering, Faculty of Engineering and Physical Sciences, University of Leeds, Leeds LS2 9JT, United Kingdom*
[d] *School of Mechanical, Aerospace and Automotive Engineering, Faculty of Engineering, Environment and Computing, Coventry University, Coventry CV1 2JH, United Kingdom*

Abstract This study aims to evaluate the performance of a photovoltaic module under some extreme climate conditions, and with a case study for Iraq. CFD model is developed for the analysis of the photovoltaic module using the commercial CFD software of COMSOL Multiphysics v5.3a for the transient conditions. The results are verified with the analytical solution to the one-dimensional non-linear energy balance equation using Matlab. The results are also compared with measurements reported in the literature for validation. The results reveal that the free convection currents in inclined and horizontal positions of the module were weaker relative to the vertical position. Also, the increase in the length of inclined photovoltaic module, up to 1.3 m, enhances the heat transfer rate. However, beyond this length, the temperature of the module becomes higher, and the convective heat transfer coefficients are reduced regardless of the inclination. In the horizontal position, the convective heat transfer rate is lower, particularly on the bottom surface of PV system.

© 2021 THE AUTHORS. Published by Elsevier BV on behalf of Faculty of Engineering, Alexandria University. This is an open access article under the CC BY license (http://creativecommons.org/licenses/by/4.0/).

1. Introduction

Over the past two decades, there has been significant growth in the production of solar PV modules, with global production in 2018 alone at 103 GW [1]. The efficiency of PV cells is, however, still low compared to other solar systems such as solar collectors (30–75%) [2–4]. The maximum solar cell efficiency for the dominant crystalline silicon is approximately 26.7%

NOMENCLATURE

Symbol	Quantity Units
A	Area, m^2
c	Specific heat capacity, $J \cdot kg^{-1}K^{-1}$
G	Global solar radiation, $W \cdot m^{-2}$
h	Heat transfer coefficient , $W \cdot m^{-2}K^{-1}$
k	Thermal conductivity, $W \cdot m^{-1}K^{-1}$
P	Power , W
L	Length , m
P_{er}	Perimeter (wetted perimeter) , m
$\dot{Q}$	Heat rate, W
$\dot{Q}_s$	Total insolation falling on PV surface, $W \cdot m^{-2}$
$\dot{Q}_v$	Volumetric heat generation rate, $W \cdot m^{-3}$
$\dot{Q}_{vd}$	Viscous dissipation, W
T	Temperature, K
t	Thickness , m
$\dot{S}$	Incident solar radiation, W
V_{PV}	Total volume of PV cells per unit length, m^3
L_c	Characteristic length, m
c_{th}	Heat capacity, $J \cdot K^{-1}$
δT_R	Diurnal temperature range, K

Greek symbols

σ Stefan-Boltzmann constant (5.67E-8), $W \cdot m^{-2}K^{-4}$

β Tilt angle , rad
ρ Density, kgm^{-3}
υ Kinematic viscosity, m^2s^{-1}

Non-dimensional numbers

Pr   Prandtl number, $c_p\mu/k$
Ra   Rayleigh number, $\frac{g\beta_{film}\Delta TL_c{}^3}{v_{flim}{}^2}$
ε Emissivity
η Efficiency
τ Solar transmissivity

Subscripts and superscripts

amb   Ambient
mpv   Mean PV (temperature)
ref   Reference
conv   Convection
Rad   Radiation
G   Glass
ted   Tedlar
tot   Total
f   Fluid

(+/-0.5%) under Standard Test Conditions (STC) where PV cell temperature and irradiance are 25 °C and 1000 W m^{-2} [5,6].

An important factor affecting the PV modules performing efficiency is the actual PV cell temperature, as it is directly proportional to the power output of the PV module. The module efficiencies are usually determined at room temperature; however, the operating conditions do vary dramatically from this. The increase in the temperature of PV module more than the STC leads to a reduction in PV efficiency. The underlying reason for this is that there is a drop in the output voltage with the increase in temperature. This is caused by the decrease in semiconductor band gap with the change in temperature, despite a slight increase in open circuit current [7]. The temperature increase causes a change in the interatomic spacing which results in the bandgap change. The reduced bandgap increases photocurrent, but not as strongly as the reduction in voltage, hence the overall reduction in conversion efficiency. For a free-standing PV module (FSPM) (for example, crystalline PV system), the increase in temperature is about 1.8 °C for every 100 W m^{-2} of power produced. For every 1 °C temperature rise, there is a decrease in power yield by about 0.5% [8]. Overheating can lead to delamination and non-homogeneous temperatures (hot spots), and a cause of damage to adhesive seals [9].

In this study, the emphasis on the mathematical studies is considered. In the literature, several attempts (e.g., [10–13]) have been made to simulate the PV cell/module temperature using explicit and implicit approaches. In the explicit approach, the direct solution for the dependent variable can be directly calculated using known variables. A list of explicit methods and a wide set of correlations were reviewed by Skoplaki and Palyvos [11] to estimate the PV temperature. For

example, Ingersoll [14] theoretically developed an expression to estimate module temperature under steady state conditions. The results indicted a good agreement for a wind speed of 1 m s^{-1}. However, a key aspect missing in that study is, that it does not consider the heat transfer which takes place in the various layers of PV module. Also, King et al. [15] provided new testing approaches for characterizing the electrical performance of PV panels and arrays. The authors utilise these tests to estimate the cell/ module temperature, however, this correlation does not capture some parameters such as the effect of mounting configuration, wind direction, thermal radiation and the analysis of heat transfer modes.

In the implicit method, the dependent variables are specified by involving unknown variables, on both sides of the equations. The solution in this case needs an iterative technique, which increases complexity, but it is more accurate. A list of implicit methods was presented by Skoplaki and Palyvos [11]. For example, a simple energy balance on the unit area of a PV module is used to implicitly predict the temperature of the PV module [16]. The correlation is a function of local wind and ambient weather including insolation and ambient temperature under real and Nominal Operating Cell Temperature (NOCT) conditions [17]. These conditions are met for ambient temperature of 20 °C, solar radiation of 800 W m^{-2}, tilt angle of 45°, wind speed of 1 m s^{-1} and zero electrical load [10,11]. In the design practice, the local wind speed varies and is seldom known with certainty. Therefore, if the actual mounting is not the same as the one used in the nominal operating cell temperature test (T_{NOCT}), the estimates given by [18] are likely to be inaccurate. Also, a major problem with the findings, yet, using this kind of method is that the authors do not consider the influence of the multiple layers of the PV module. Some other models are based on empirical correlations [19–21].

These correlations are functions of the ambient temperature (T_{amb}), type of semiconductor material and incident solar radiation (G). For example, Lasnier and Ang [20] developed a formula used for a standard polycrystalline silicon (pc-Si) PV cell. Kalogirou and Tripanagnostopoulos [21] developed an expression for an amorphous silicon (a-Si) PV cell. It should be noted that some parameters were not captured in those correlations, such as the wind effect and heat loss coefficient. Similarly, a number of studies (e.g., [22–24]) were carried out to evaluate the PV panel performance using CFD modelling.

In contrast to previous studies, this paper aims at an improved prediction of the PV module and thermal evaluation under extreme weather conditions, taking into account the comprehensive module design parameters. The effects of PV module length, inclination and influence of the maximum possible module temperature are considered. These are examined under the worst-case scenarios of hot climatic conditions (the case of Iraq) and natural convection. Numerical models are developed to adapt to the new case design and conditions, and they are validated against experimental data. The proposed models in this discourse incorporate parameters (for example, PV module length, tilt angle, worst weather conditions and influence of the maximum possible module temperature) that have not been intensively studied in the literature to date.

2. Module description

The photovoltaic technology chosen in this work is the polycrystalline British Petroleum (BP) Solar BP 585 which typically consists of five layers: the glass cover, PV cells, encapsulation foil, a back sheet layer (Tedlar) and metal frame [25]. The material and operating properties of this PV module is portrayed in Table 1 and Table 2. In Table 1, t is the thickness of PV cell (mm), ρ is the density (kg m^{-3}), k is the thermal conductivity (W m^{-1} K^{-1}) and c is the specific heat capacity (J kg^{-1} K^{-1}). The heat capacity of the PV layer module material (c_{th}) refers to its ability to absorb and store heat.

The mass of the PV layers is the main parameter in determining the amount of c_{th}, which can be calculated as:

$$c_{th} = \rho c A_{pv} t, \tag{1}$$

The electrical power generation from a PV module can be estimated as [26,28]:

$$P_{PV} = I_m V_m = FF I_{sc} V_{oc} = \frac{\eta_{PV} A_s \tau_{g-EVA} G \alpha_{PV}}{V_{PV}} \tag{2}$$

where I_m and V_m are voltage and current at the max power point respectively, FF is the filling factor, I_{sc} is the short circuit current, V_{oc} the open circuit voltage [26], A_s is the total exposed surface area of PV module, V_{PV} is the total volume of PV cells and the product $(\tau_{g-EVA} G \alpha_{pv})$ is the solar energy absorbed by the PV laminate, where α_{pv} is the absorptivity of the silicon and τ_{g-EVA} the combined transmissivity of the EVA layers and the glass, and η_{PV} is the module efficiency calculated as in [29]:

$$\eta_{PV} = \eta_{\mathrm{ref}}\left[1 - \beta_{ref}\left(T_{mpv} - T_{\mathrm{ref}}\right)\right] \tag{3}$$

where η_{ref} is reference efficiency and β_{ref} is temperature coefficient of power (K^{-1}), which are provided by the PV manufacturer at STC. Equation (2) can also be used as a reference system PV/Ref (base data/baseline) to compare with the hybrid PV/T performance. The prediction of solar cell/panel operating temperature (T_{mpv}) of FSPM is essential because it is the dominant parameter to estimate the module efficiency. The electric power output is the most significant to the system performance – unlike the efficiency, which is greatly influenced by the ambient temperature.

3. The model

A simplified CFD model is developed under steady state and dynamic conditions using COMSOL Multiphysics® version 5.3a (a finite element method (FEM) tool). A transient solver is used to enhance the accuracy of the model. To input meteorological data including ambient temperature and solar radiation, an interpolation technique (built in COMSOL) of the cubic spline function type is used. The governing equations, assumptions boundary conditions are expressed in the following sub-sections. A diagram of the PV module used in this study is shown in Fig. 1.

In Fig. 1, five temperature locations were illustrated as follows: the temperature of the top/front surfaces T_1, the temperature of the interface between the glass and EVA layers T_2, the temperature of the PV cell layer (the same as the interface temperatures between the upper and lower EVA layers) T_3, the temperature of the interface between the EVA and Tedlar layers T_4, and the temperature of the bottom/rear surfaces T_5.

3.1. Assumptions

The short-wave radiation falling on the PV module is converted into two forms, electrical and thermal waves. Some of this radiation is dissipated to the surroundings as thermal losses in the form of longwave radiation and by convection.

Table 1 Material properties of the PV module layers (BP 585)[26].

| Layer	t	k		c	μ	τ	t/k
PV glass	3	1.8	3000	500	0.84	0.91	1.7×10^{-3}
EVA	0.5	0.35	960	2090	–	–	1.4×10^{-3}
PV cells	0.3	148	2330	677	0.91		2.0×10^{-6}
Tedlar	0.5	0.2	1200	1250	0.87	–	2.5×10^{-3}

Table 2 Operating properties of the PV module BP 585 [26,27].

Electrical data at STC		Thermal ratings		Material data	
Module maximum power (P_{max})	50 W	Operating temperature range	$-40 \sim 85$ °C	Panel dimensions (L w)	0.666 m × 0.606 *m*
Voltage at maximum power (V_{mmp})	17.89 V	Temperature coefficient of P_{max}, (β_{ref})	-0.41%/°C	Cell type	Polycrystalline
Current at maximum power (I_{mmp})	2.8 A	Temperature coefficient of (V_{oc})	-0.31%/°C	Cell number	36
Open circuit voltage (V_{oc})	21.77 V	Temperature coefficient of (Isc)	0.058%/°C	Glass type	Tempered, high transmittance, low iron
Short circuit current (I_{sc})	3.04 A	Panel efficiency $\eta_{pv,T_{ref}}$	12.35%	Encapsulant type	EVA
Note: data are presented at standard conditions, AM 1.5, 1000 W m^{-2}, 25 °C.					

The remainder is converted into electrical power. The following assumptions are made:

- 1D heat conduction has been assumed for the current study, because the aspect ratios of the width and length of the module to the thickness of the layers lie between 200 and 2000 [25].
- There are temperature gradients across all the layers except for the PV layer itself. The equivalent thermal resistance t/k of the PV layer is three orders of magnitude less than those values of the other layers (see Table 1). Fig. 2 illustrates the equivalent thermal circuit for the heat flows through the PV laminate.
- The effect of accumulated dust, dirt and fouling factor is insignificant [18].
- The transmissivity of the glass and the EVA is 0.91 [25,30].
- The ambient temperature is homogeneous.

- Ohmic heating (resistive heating) in the PV cells is regarded as negligible, which implies that the temperature distribution along the PV module is uniform [30].
- Following [26,30], the ground and ambient temperatures are assumed equal.
- The radiative exchange from the top/front surface is to the sky (T_{sky}), which taken to be the ambient temperature. Similarly, the bottom/rear of the PV laminate is considered a radiative exchange surface to the ground.
- Both outer surfaces of the PV panel are subjected to only free convection conditions to represent the worst case scenario [30].
- The PV system is completely sealed and bonded. This means the multiple reflections and transmissions between the components are considered negligible [22].
- The shadow effect is ignored [18].
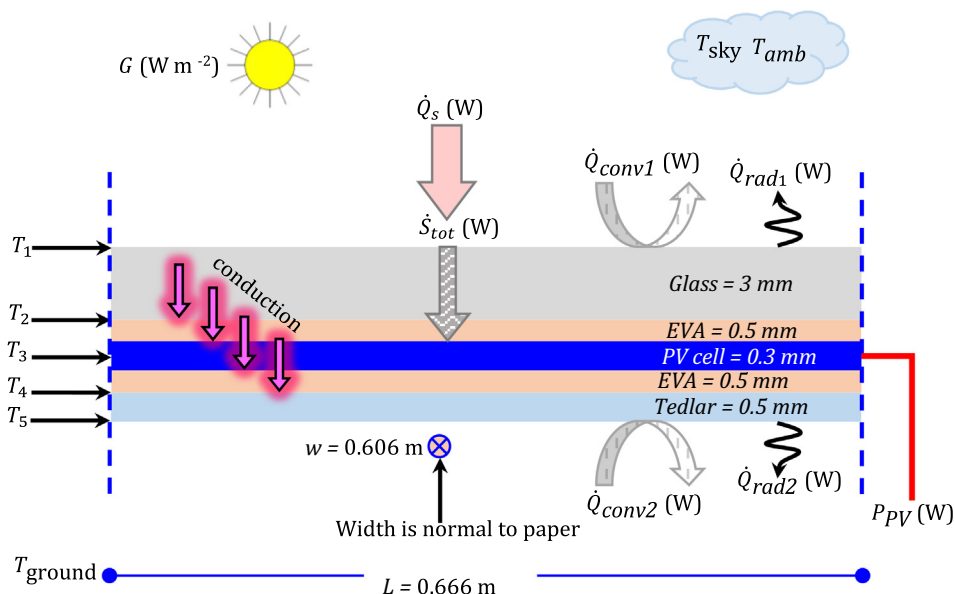
Fig. 1 Schematic of the main heat transfer modes taking place at various locations of the PV module.
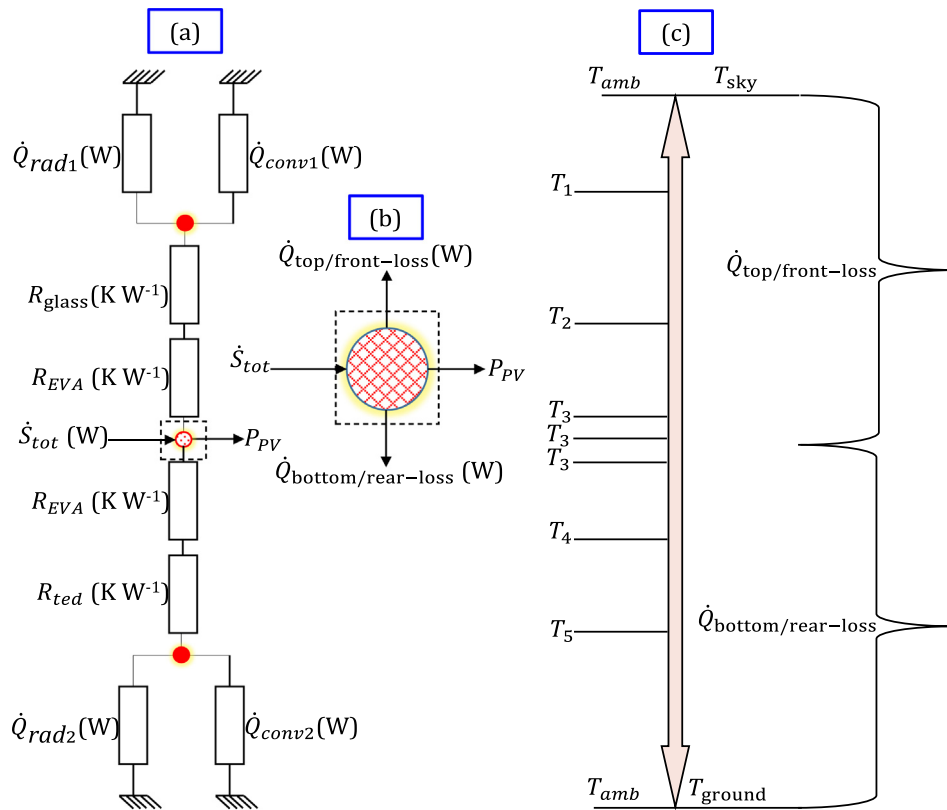
Fig. 2 Equivalent thermal circuit of the PV module.

- Perfect bonding between the layers of the PV module is assumed which means that thermal contact resistance between them is negligible [31,32].
- The thermal conductivity of the PV layers is temperature independent.
- The PV layer material are homogeneous and isotropic.
- The physical air properties are dependent on temperature.

3.2. Basic equations

The boundary conditions are set as close as possible to real conditions. The surface-to-surface radiation module is used with an 'External Radiation' node to simulate the incoming solar radiation (COMSOL terminology are placed in quotes from here on). A 'Diffuse Surface' node is also added to model absorption and emission from the heated surfaces to the surroundings, as [33]:

$$q_{\text{rad}} = \varepsilon\sigma\left(T_s^{\,4} - T^4\right), \tag{4}$$

where T is a surrounding temperature (K) and T_s is a surface temperature (K). The transient conjugate heat transfer equation is used, with a heat generation and translational motion of the parts as:

$$\frac{D(\rho cT)}{Dt}.\nabla T = \nabla.\left(k_{x,y,z}\nabla T\right) + \dot{Q}_v \tag{5}$$

where ρ is the density of PV layers (kg m^{-3}), c is the heat capacity of PV layers at constant pressure (J kg^{-1} K^{-1}), $k_{x,y,z}$ is the thermal conductivity of the PV layers (W m^{-1} K^{-1}) $\times$, y and z directions and assumed isotropic ($k_x = k_y = k_z$). $\dot{Q}_v$ is the volume heat source or sink. Three cases are considered in this study as follows: In terms of PV cells where the conditions are: 1D, steady state conditions, the generated electrical power which can be treated as a heat sink ($\dot{Q}_v$) and a stationary PV cells, Equation (5) reduces to:

Table 3 Optimum tracking angles β (degrees) values for Fallujah city.

Month	Jan	Feb	Mar	Apr	May	Jun	Jul	Aug	Sep	Oct	Nov	Dec
β	56	45	27	11	2	1	1	8	22	39	53	61
Day	31	28	31	30	31	9	1	1	1	1	1	1
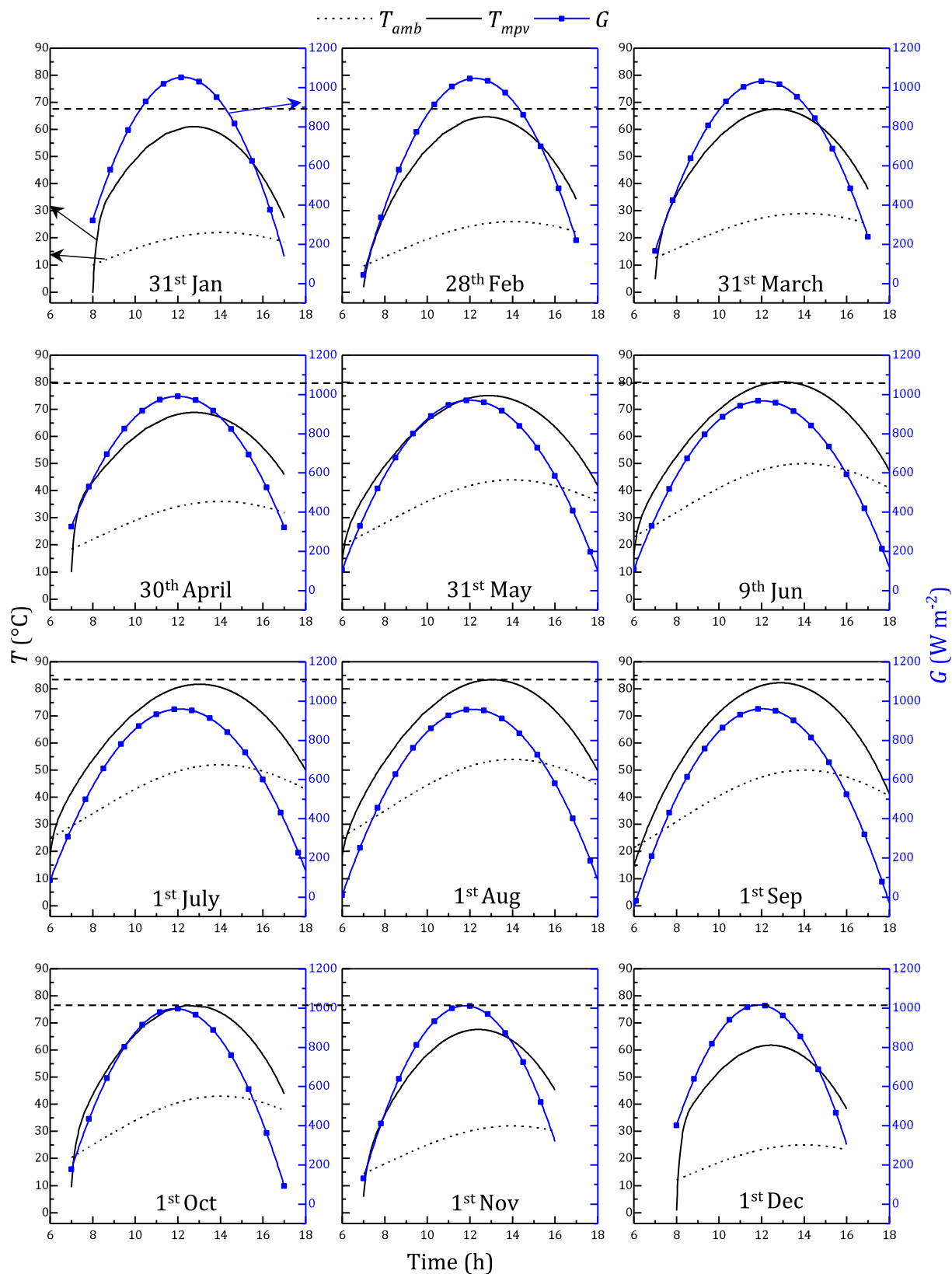
Fig. 3 Average PV module temperatures, insolation and ambient versus measurement time of the hottest days in each month in Fallujah city. The worst cases (the maximal insolation and ambient temperatures in each month) were implemented into transient and free convection CFD models.
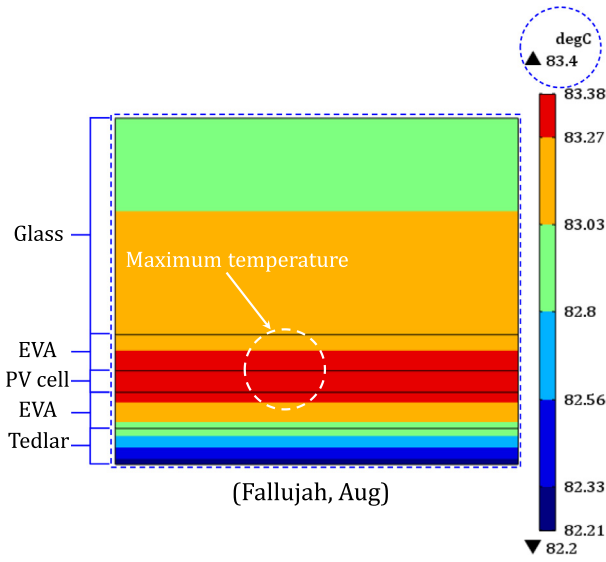
Fig. 4 Typical temperature profile (°C) of the standard PV module on 1st Aug at 13:00 in Fallujah city, predicted using a free convection and transient CFD model (time step is 1 min).

$$\frac{\partial}{\partial x}\left(k_x \frac{\partial T}{\partial x}\right) + \frac{\partial}{\partial y}\left(k_y \frac{\partial T}{\partial y}\right) = \dot{Q}_v \qquad (6)$$

Concerning other PV module layers (i.e. EVA, Tedlar and glass) in which the conditions are, 1D semi-infinite solid, steady state conditions a stationary PV layers, Equation (5) is simplified to:

$$\frac{\partial}{\partial x}\left(k_x \frac{\partial T}{\partial x}\right) + \frac{\partial}{\partial y}\left(k_y \frac{\partial T}{\partial y}\right) = 0. \qquad (7)$$

With respect to PV cell, 1D semi-infinite solid, transient conditions where the heat generated as a heat sink, $(\dot{Q}_v)$ and a stationary PV cells, Equation (5) becomes:

$$\rho c \frac{\partial T(x,y,t)}{\partial t} = \frac{\partial}{\partial x}\left(k_x \frac{\partial T}{\partial x}\right) + \frac{\partial}{\partial y}\left(k_y \frac{\partial T}{\partial y}\right) - \dot{Q}_v \qquad (8)$$

Concerning other PV layers (EVA, Tedlar and glass) the system is 1D semi-infinite solid, transient conditions a stationary PV layers, the governing heat transfer equation becomes:

$$\rho c \frac{\partial T(x,y,t)}{\partial t} = \frac{\partial}{\partial x}\left(k_x \frac{\partial T}{\partial x}\right) + \frac{\partial}{\partial y}\left(k_y \frac{\partial T}{\partial y}\right). \qquad (9)$$

3.3. Numerical verification

One dimensional (1D) analysis is carried out to evaluate the electrical and thermal performance of the PV module (see Fig. 1). This analysis is conducted, using Matlab software, to verify the CFD results. A simple energy balance method is used in this analysis, with the same assumptions are made for the CFD model. The heat balance over the PV cell layer is estimated using the following expression:

$$\dot{S}_{tot} = P_{PV} + \dot{Q}_{top/front-loss} + \dot{Q}_{bottom/rear-loss}, \qquad (10)$$

where the total incident radiation reaching the PV cell is given as follows:

$$\dot{S}_{tot} = \frac{G A_s \tau_{g-EVA} \alpha_{pv}}{V_{PV}}. \qquad (11)$$

The electrical power generated in the cell at the temperature T_3 is given by the following expression:

$$P_{PV} = \eta_{PV} \dot{S}_{tot}. \qquad (12)$$

The heat loss from the top/front of the cell is by conduction through the EVA and glass layers, and finally, by convection and radiation from the glass surface and is represented by the following equations:

$$\dot{Q}_{top/front-loss} = A_s \frac{T_3 - T_2}{(t_{EVA}/k_{EVA})} = A_s \frac{T_2 - T_1}{(t_g/k_g)}$$
$$= h_{free1} A_s (T_1 - T_{amb}) + \sigma \varepsilon_g A_s (T_1^4 - T_{amb}^4). \qquad (13)$$

In a similar manner, the heat loss from the bottom/rear of the cell can be presented as follows:

$$\dot{Q}_{back/rear-loss} = A_s \frac{T_3 - T_4}{\left(\frac{t_{EVA}}{k_{EVA}}\right)} = A_s \frac{T_4 - T_5}{\left(\frac{t_{ted}}{k_{ted}}\right)}$$
$$= h_{free2} A_s (T_5 - T_{amb})$$
$$+ \sigma \varepsilon_{ted} A_s (T_5^4 - T_{amb}^4). \qquad (14)$$

Empirical correlations are used to estimate the free convective heat transfer coefficients on the top/front and bottom/rear PV module surfaces for both the CFD model and numerical analysis. These are classified based on the inclination. Churchill and Chu [34] have recommended the following correlation to apply over the entire range (laminar and turbulent regions) of Rayleigh number (Ra_{L_c}):

$$h_{free} = \left(\frac{k_f}{L_c}\right)\left(0.825 + \frac{0.387 \ \sin\beta \ Ra_{L_c}^{1/6}}{\left(1 + \left(\frac{0.492 k_f}{c_{pf}\mu_f}\right)^{9/16}\right)^{8/27}}\right)^2. \qquad (15)$$

For turbulent flow, it is found that natural convection heat transfer coefficient (h_{free}) is not sensitive to the inclination angle (β). According to [34], h_{free} in the laminar regime should be estimated using of the following amendment to Equation (15) for a greater accuracy:

$$h_{free} = \left(\frac{k_f}{L_c}\right)\left(0.68 + \frac{0.67 \ \sin\beta \ Ra_{L_c}^{1/4}}{\left(1 + \left(\frac{0.492 k_f}{c_{pf}\mu_f}\right)^{\frac{9}{16}}\right)^{\frac{4}{9}}}\right) \text{ when } Ra_{L_c} \leq 10^9,$$

where L_c is the length of the PV module and β is the tilt angle (the module angle between the horizontal and vertical positions). The correlations are valid for $30° \leq \beta \leq 90°$.

According to [34,35], the correlations for inclined walls (i.e., Equations (15) and (16)) are only satisfactory for the topside (upper surface) of a cold plate or the downside (bottom surface) of a hot plate. Hence, these correlations are not recommended for the downside of a cold face nor for the topside of a hot plate. Since the application of inclined PV systems to the top and down sides of a hot plates does not match the aforementioned literature cases, some deviations owing to this is suggested. In this study, the tilt angles (in the range $30° - 90°$) and the horizontal position are both studied. The thermal effects of free convective boundary layers can change
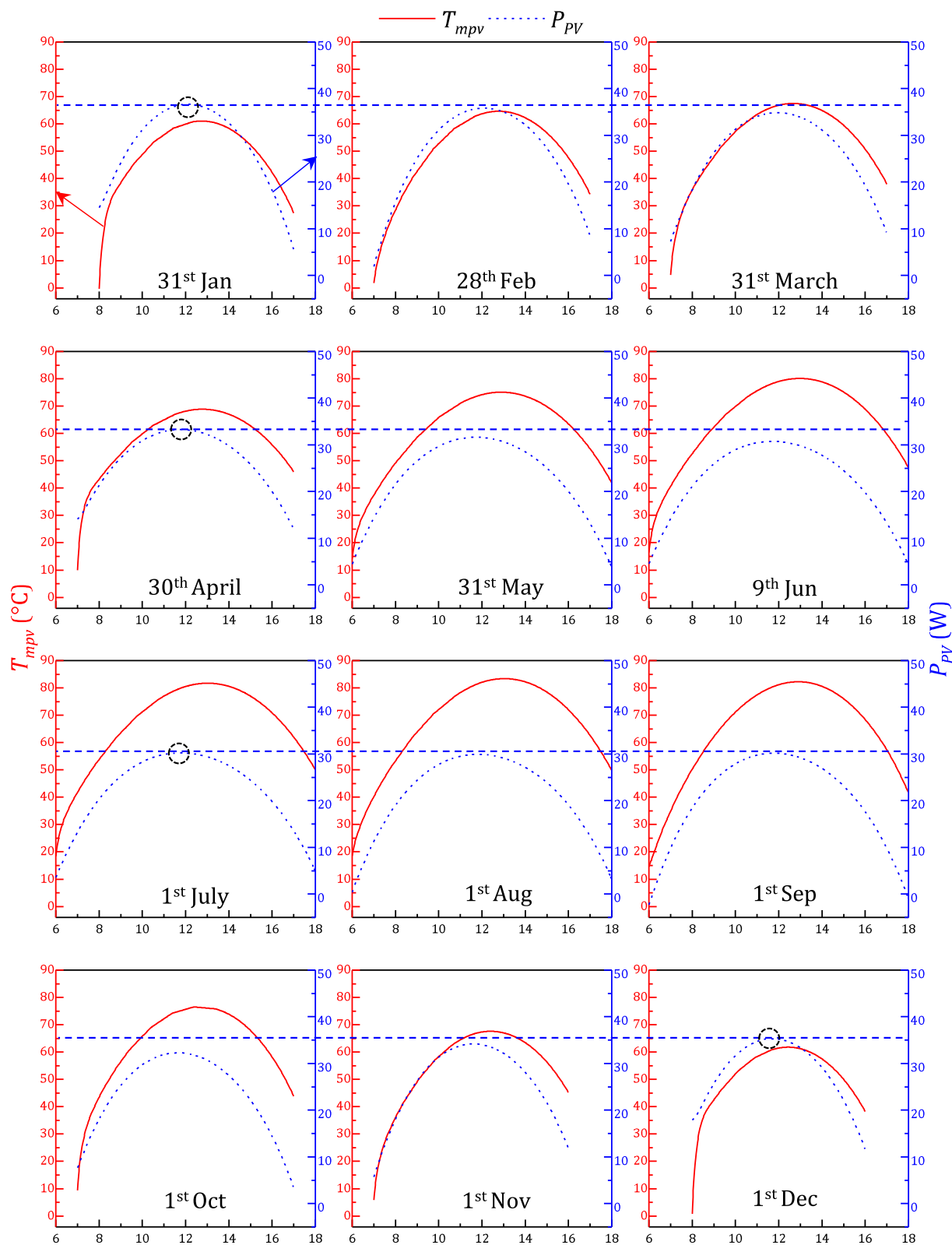
Fig. 5 Average PV module temperatures and electric power generation versus measurement time of the hottest days in each month in Fallujah city. The worst cases (the maximal insolation and ambient temperatures of each month) were implemented into our transient and free convection CFD models. The transient simulation time step is 1 min.
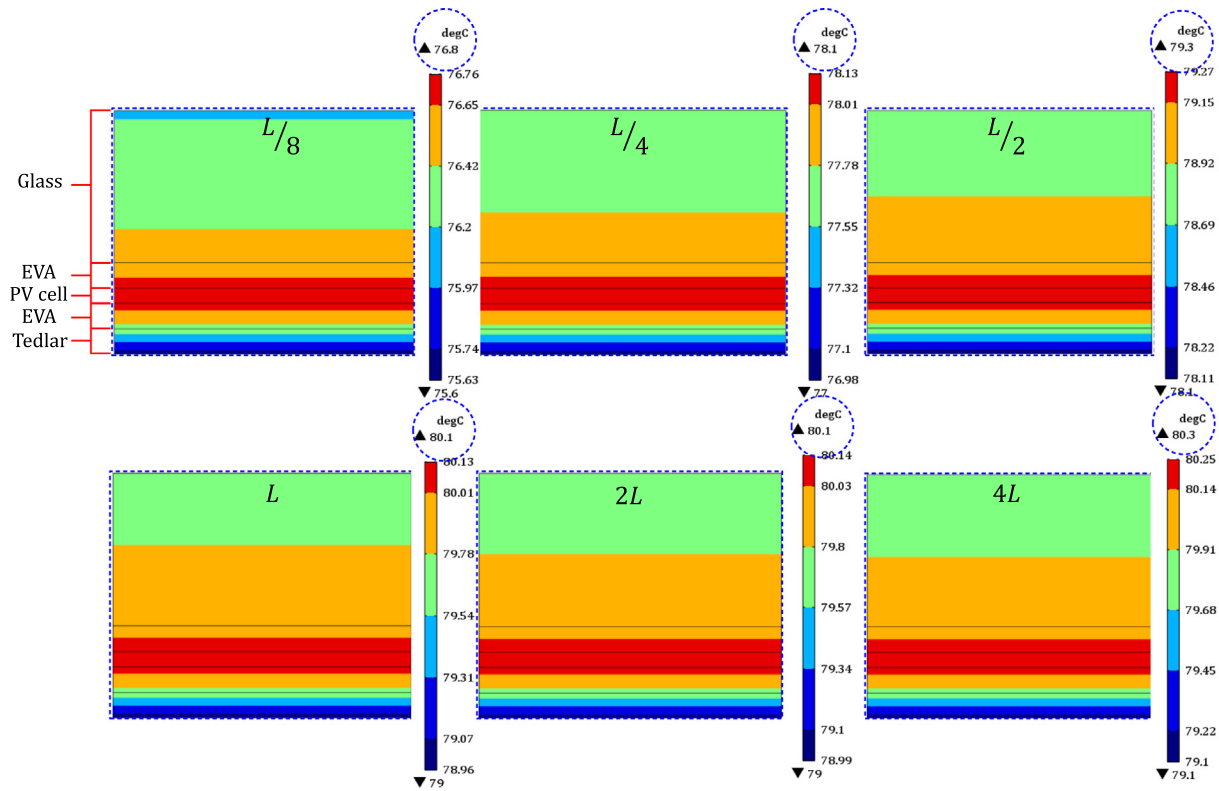
Fig. 6 Temperature profiles (°C) of the standard PV module on 1st June at 13:00 in Fallujah city, predicted using the free convection and transient CFD model for various PV module lengths (time step is 1 min).

according to the surface orientation as: inclined, vertical and horizontal surfaces. However, correlations representing these developing boundary layers and the equivalent variable heat transfer coefficients are not available in the literature, except for the vertical wall. Hence, uniform heat transfer coefficients are considered in these studies. In the case of horizontal position (hot surface upward, i.e. the topside hot plate), the convective heat transfer coefficients are calculated for laminar and turbulent flows, respectively, as follows [35]:

$$h_{\text{free}} = (k_f/L_c) \ 0.54 \ \text{Ra}_{L_c}^{1/4} \ \left\{\text{for } 10^4 \leq \text{Ra}_{L_c} \leq 10^7, \ \text{Pr} \geq 0.7\right\} \tag{17}$$

$$h_{\text{free}} = (k_f/L_c) \ 0.15 \ \text{Ra}_{L_c}^{1/3} \left\{\text{for } 10^7 \leq \text{Ra}_{L_c} \leq 10^{11}, \ \text{all Pr}\right\} \tag{18}$$

Equations (17) is used for the case of laminar flow, while Equation (18) is used for the case of turbulent flow. In the case of the downside hot plate (facing downward), the following approximation is used [33]:

$$h_{\text{free}} = \left(k_f/L_c\right) \ 0.27 \ \text{Ra}_{L_c}^{1/4} \ \left\{\text{for } 10^5 \leq \text{Ra}_{L_c} \leq 10^{11}\right\} \tag{19}$$

The non-linear algebraic equations are solved numerically using fsolve, a built-in Matlab solver. For more information, the numerical algorithm is illustrated in Appendix A. The characteristic length is determined as [33]:

$$L_c = \frac{A_s}{P_{er}} = \frac{wL}{2(w+L)} \ \text{for a horizontal surface,}$$

$L_c = L$ for vertical and inclined surfaces.

The empirical correlations used to estimate the free convective heat transfer coefficients on the upper and bottom PV module surfaces have been presented earlier (Equations (15) to (19)). These equations are used for both CFD modelling and 1D numerical analysis.

4. Results

The CFD simulation is carried out for the PV module based on the experimental data obtained in Fallujah City as a case study for validation. Fallujah is in West Iraq at 33.34° N, 43.78° E and 47 m above sea level (MASL). This city is chosen because it gains a relatively great amount of annual average insolation of 5.8 kWh·m^{-2} day^{-1} [36]. The thermal evaluation has been conducted under free convection and peak incident solar radiation. Under such conditions, the performance of the PV module is evaluated under the worst-case scenario (i.e., highest expected PV panel temperature influencing its performance).

4.1. Impacts of ambient conditions

The optimum tracking angles (the angles resulting in maximum solar radiation on an inclined surface) (β) are presented in Table 3 [37]. The variation of the average PV module temperature of the CFD model is evaluated under the worst case scenario (i.e. the maximum solar radiation and ambient temperature for a day in each month) for each month over a year

in Fallujah city under transient and under free convection conditions (time step is one minute and $L = 0.666$ m), as shown in Fig. 3. It is obviously seen that the PV panel temperature increases with an increase in the insolation and ambient temperature.

In Fig. 3, the maximum module temperature is 83.4 °C in August (see also Fig. 4 for temperature contour) in which the ambient temperature is at the maximum value throughout the year (54 °C). Referring to Fig. 4, it should be noted that the maximum temperature is in the PV cell layer because the electrical power is generated in this layer.

The impact of average PV module temperature on its module's power output for 12 months under free convection and transient conditions in Fallujah is illustrated in Fig. 5. The trends in this figure reveal that the generation of PV power follows the PV panel temperature as the PV panel temperature and intensity of solar radiation are the main factors that influence PV power generation. Therefore, the maximum instantaneous (not for whole day) power generation is in January despite the insolation in June is almost same magnitude for the same day (see Figs. 3 and 5). This result, however, may not be generalised for whole days in January and June, it depends on the two aforementioned factors (ambient temperature and insolation). It can be deduced that lower ambient temperature and higher insolation values lead to better PV performance, which can be clearly seen in June, Fallujah. The variations of PV module efficiency and electric power generation throughout the year are presented in Appendix C, Fig. C1.

4.2. Impacts of length and tilt angle

The effects of different lengths, L/8, L/4, L/2, L, 2L "and" 4L, of the PV module in a horizontal position on the average temperature are presented in Fig. 6 for a typical hot day (1st June at 13:00) in Fallujah. There is a slight increase in temperature with increasing lengths up to L, but after L the temperature is almost constant. This phenomenon is attributed to the limited buoyancy force, which is normal to surface, and convection currents. To justify these behaviours, for the shorter lengths, the free convection laminar flow is developing from the extreme lengthwise edges of the module and the path length is relatively short before a central plume forms and flows upwards away from the surface. The convective heat transfer rate is greater in these shorter path lengths of developing flow than that of the fully developed flow at later positions. Eventually the flow will become fully laminar, and the heat transfer rate becomes less. Hence, the increase in the average temperature up to L/2 [38]. There is no further enhancement in heat transfer after length ($L = 0.666$ m) and so, the laminar flow will have reached the point of transition to turbulent flow or flow separation.

In the bottom surface of the PV module, the PV plate obstructs airflow, apart from the PV panel edges where the flow is free to ascend. Due to this obstruction, the flow moves horizontally, then it rises from the edges of the PV panel, and the convective heat transfer rate is inefficient. Conversely, on the top PV surface, the heated fluid moves freely, inducing strong natural convection currents and thus, the heat transfer rate is enhanced.

The convection currents are weak because the buoyancy force is normal to surface. However, at the bottom surface
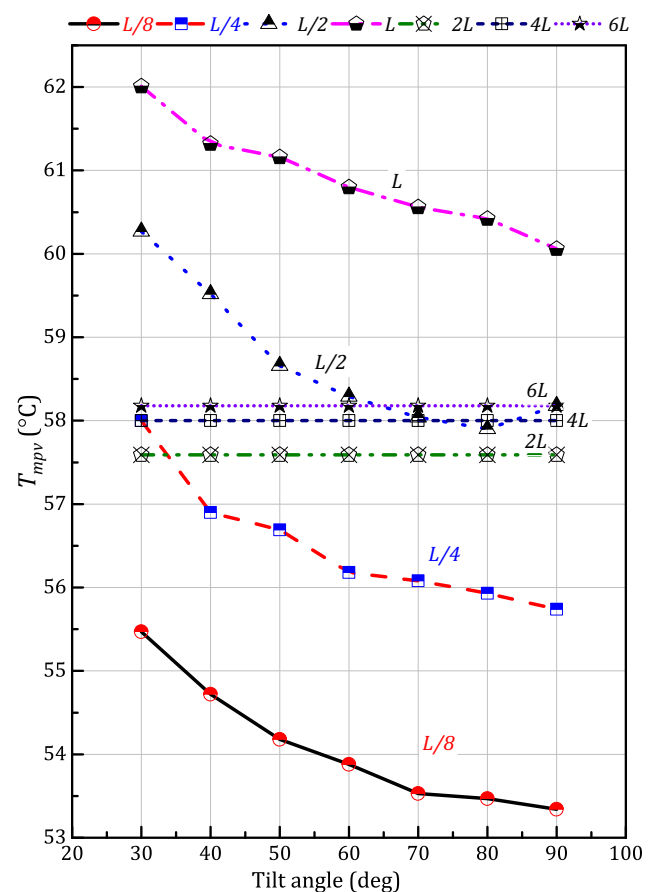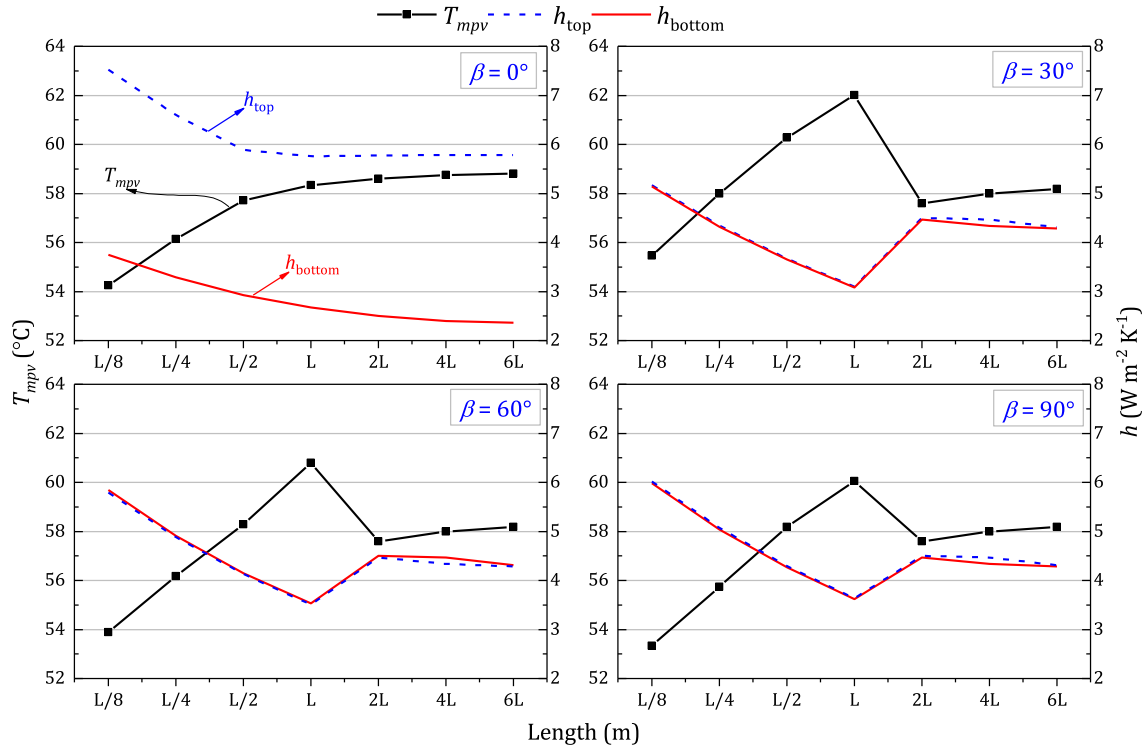

Fig. 7 Tilt angle (in the range $30° - 90°$) versus average PV module temperature with different lengths, predicted using the CFD model for a typical 31st January at 13:00 in Fallujah city.

of the PV module, the flow is obstructed apart from the module edges where the flow is free to ascend. Owing to this obstruction, the flow moves horizontally, then it rises from the edges of the PV panel and the overall convective heat transfer rate is inefficient [39]. Conversely, on the top surface of the PV module, the heated fluid moves freely, inducing strong natural convection currents and thus, the heat transfer rate is enhanced compared that on the bottom surface, as illustrated in Appendix C (Table C 1).

The impact of PV module length on its temperature is shown in Fig. 7. The module lengths L/8, L/4, L/2, L, 2L, 4L, and 6L on its temperature are studied for inclinations $30° - 90°$ in Fallujah city on 31st January at 13:00. It is expected that the convection currents are weaker and the heat transfer rate is lower relative to the vertical position [40]. This is particularly seen in the 30° inclination for up to L long module, knowing that the inclination angles between 0° and 30° are not considered in this study due to the limitation of Equations (15) to (19). In the case of an inclined PV module, the buoyancy and gravity force act vertically on a unit volume of the fluid boundary layer. This force can be resolved into two components, parallel and normal to the module plate. Noting that the parallel force that drives the motion is reduced at lower tilt angles down to 30°; that means the convection currents

Fig. 8 Convective heat transfer coefficients at the top and bottom surfaces and the average PV module temperatures versus lengths, predicted using the CFD model for various inclinations on 31st January at 13:00 in Fallujah city.

become weaker. For higher tilt angles, above 30°, the airflow is motivated due to the bouncy effects; hence, reducing the module temperature.

Also, from the data shown in Fig. 7, the PV module temperatures (T_{mpv}) increase with increasing length up to L for inclinations 30°-90°. This is because the flow is expected to be laminar and is thus sensitive to changes in length and inclination [34]. It can also be seen that the module temperatures in lengths $L/8$ and $L/4$ are lower than $L/2$ and L for the same inclinations. This is most likely owing to the flow in small lengths

not being fully developed. Therefore, the rate of heat transfer in the developing region is greater relative to the fully developed ones (longer lengths) [38] (see Appendix C, Table C1, for further illustration). Following [41], one can see that the inclination effects on T_{mpv} become insignificant for long modules $(> L)$ due to the flow transition from laminar to turbulent.

Fig. 8 reveals the influence of the convective heat transfer coefficients at the bottom (h_{bottom}) and top (h_{top}) surfaces of
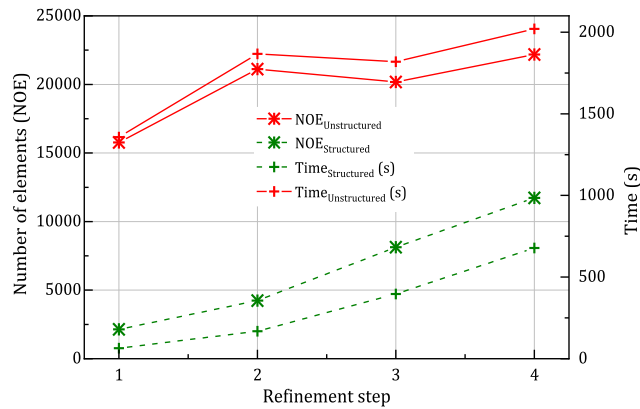
Fig. 9 Number of mesh elements versus conducted refinement steps for the structured and unstructured meshes of standard PV unit. See Appendix B for more details about the mesh specifications.
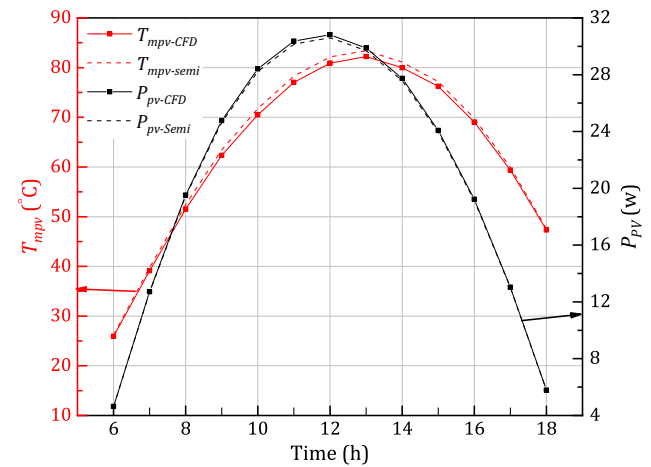
Fig. 10 Average PV module temperature and generated power versus time (hour) in a typical hot day in July in Fallujah city. The results are presented in comparison between the CFD model and semi-analytical approaches.
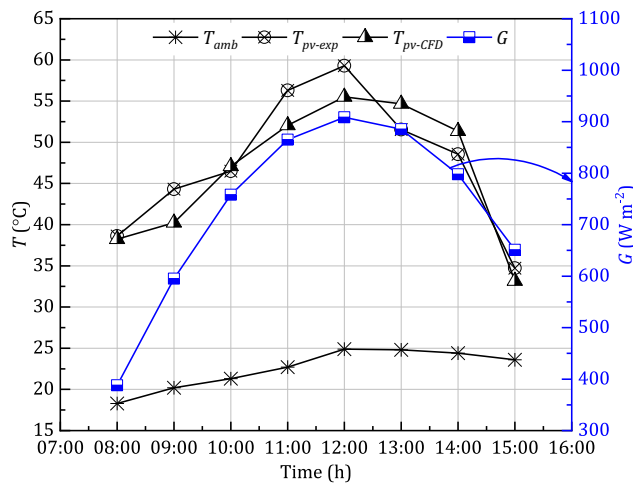
Fig. 11 Average PV module temperature versus time (hour), predicted using our CFD and compared to experimental data of [29]. The measured ambient temperature and solar radiation are shown at the same measurement hours.

the PV module on its temperature at three typical inclination positions (0°, 30°, 60° and 90°). In the case of the horizontal orientation ($\beta = 0°$), h_{top} is greater than h_{bottom}. This difference is attributed to the fact that the air at the bottom surface is obstructed by the PV panel before ascending from their edges. While at the top surface, the flow moves freely and is driven by rising air parcels from the top surface. This is replaced by ascending warmer air from the ambient, leading to $h_{top} > h_{bottom}$.

4.3. Grid independence test

Two mesh element types are used in our model, the first is simple linear free unstructured triangular mesh and the second is quadrilateral structured mesh. The mesh test analysis is conducted to obtain a proper element type and size, improve accuracy, and limit the overall computation time. Five criteria are taken into account, which are physical Random-Access Memory (RAM) in Giga bytes (GB), solution time in seconds, number of elements (NOE), degrees of freedom (DOF) and minimum element quality (MEQ).

The key features of the mesh independence test analysis for a standard PV system using structured and unstructured mesh elements are shown in Fig. 9 for a typical hot day on 1st July. For details about the MEQ of structured mesh, RAM, run time and NOE, see Appendix B. It is found that using the structured mesh has significantly contributed to limiting the run time and RAM, respectively, from 1357 sec and 6.73 GB to 64 sec and 1.54 GB and will therefore be adopted.

It should be noted that the maximum percentage error (relative to the finest mesh) obtained is approximately 0.5%, even when using high mesh density (e.g., Trial 4). This is attributed to:

1. The model is assumed equivalent to a 1D semi-infinite solid, because of the limitation of the software to represent

the solar radiation in case 1D representation using Comsol v5.3a.
2. Ignoring the thermal edges losses since the aspect ratio (length/frame thickness) is ~ 1000. In other words, the sides of the PV module are considered to be adiabatic [42].
3. The thicknesses of the PV layers are comparatively small.
4. The thermal conductivity of the PV layers is also relatively high.
5. The model is dominated by the conduction mode.
6. The Correlations (15) to (19) are used to calculate heat transfer coefficients by free convection for the top/front and bottom/rear PV module surfaces; i.e. the values of these coefficients are uniform in the model; however, in reality, they might change along the PV module specifically in the vertical and inclined states [35,43].

4.4. Comparison to numerical analysis

The verification is between the numerical (semi-analytical) and developed steady-state CFD models. Fallujah weather data are considered to evaluate the PV module temperature and electrical power generated for a typical day in July. The CFD model is semi-infinite solid domain, and the numerical analysis is a 1D domain. The two models showed a close agreement as can be seen in Fig. 10. The following reasons are sought to explain the results:

1. The CFD model can be assumed 1D semi-infinite solid as justified earlier in point 1 Section 4.2 (grid independence test).
2. The PV layer thickness is relatively small, while the thermal conductivity is comparatively high.
3. The similarity in the representation of the heat transfer modes. For example, the external heat transfer by free convection is represented in the two models using the same empirical equations.

4.5. Comparison to experimental data

The CFD developed model is validated with available experimental results in Fallujah, Iraq [29]. With respect to the validation in Fallujah, the current numerical result is validated in terms of average PV panel temperature, as shown in Fig. 11. This figure displays the incident solar radiation, ambient temperature and PV panel temperature versus time 08:00–15:00 hrs on 24th March 2011. The CFD model was developed under steady state conditions. One can see that the PV panel temperature increases gradually with the solar radiation and ambient temperature from sunrise to reach a peak value at the solar noon (12:00hr) and then reduces until sunset. The results reveal that a good level of conformity is obtained between the current CFD model and experiments with the maximum temperature difference of approximately 4 °C. This difference may be because of the following (including but not limited to) possibilities:

• The accuracy in measuring the ambient temperature and incident solar radiation.

- The difficulty in estimating the wind effect/wind direction accurately.
- Dust accumulation.
- The CFD model is simplified to a semi-infinite solid problem, whereas the physical system is 3D.
- Our model is based on quasi-steady assumption, but in real life, the system is time-dependent.

5. Conclusions

In this work, the PV module temperature profile was predicted and examined using 1D mathematical and semi-infinite solid CFD models and validated against experimental data. Some extreme weather conditions were taken into account, such as the highest intensity of solar radiation for each calendar month. Furthermore, detailed monthly case studies were considered based on the average daily conditions for a year. In light of the present study, the following findings have been concluded:

- The convection currents in inclined and horizontal surfaces are weaker relative to the vertical surface; thus, the rate of heat transfer is lower.
- In the case of inclined PV systems, the increase of PV lengths (up to 2L) enhances the heat transfer rate. After 2L , the convective heat transfer coefficients decrease, and the PV temperature increases regardless to the inclination of PV system.
- Increasing the length of the PV panel may not be feasible or affordable because the PV array blocks could shade further arrays. Also, this might increase the cost of installation and price of the base frame (in the expense of cost and difficulty of installation).
- In the case of horizontal orientation, the convective heat transfer rate is relatively low. This was more noticeable at the bottom surface of the PV system.

- The effect of inclination becomes more noticeable in the shorter length (i.e., laminar region), but this effect dissipates in the longer (turbulent) region.
- Lower ambient temperature and higher insolation values lead to better PV performance, and this can be seen in Fallujah in January.

Declaration of Competing Interest

The authors declare that they have no known competing financial interests or personal relationships that could have appeared to influence the work reported in this paper.

Appendix A. Numerical implementation methods

The numerical algorithm is illustrated in a logic flow chart of Fig. A1. The first step is to specify the input parameters including ambient, operating and geometrical conditions (see step 1 and 2).Fig. B1.

Secondly, temperature of the PV layers are initially assumed to be at $\left(\tilde{T}_1, \tilde{T}_2, \tilde{T}_3, \tilde{T}_4, \tilde{T}_5 \right)$. In contrast to previous studies where free convective heat transfer coefficient h_{free} is assumed constant, we use empirical correlations to estimate h_{free} , determined from Correlations (17)–(19) and the convective and radiative heat losses from the top/bottom and front/
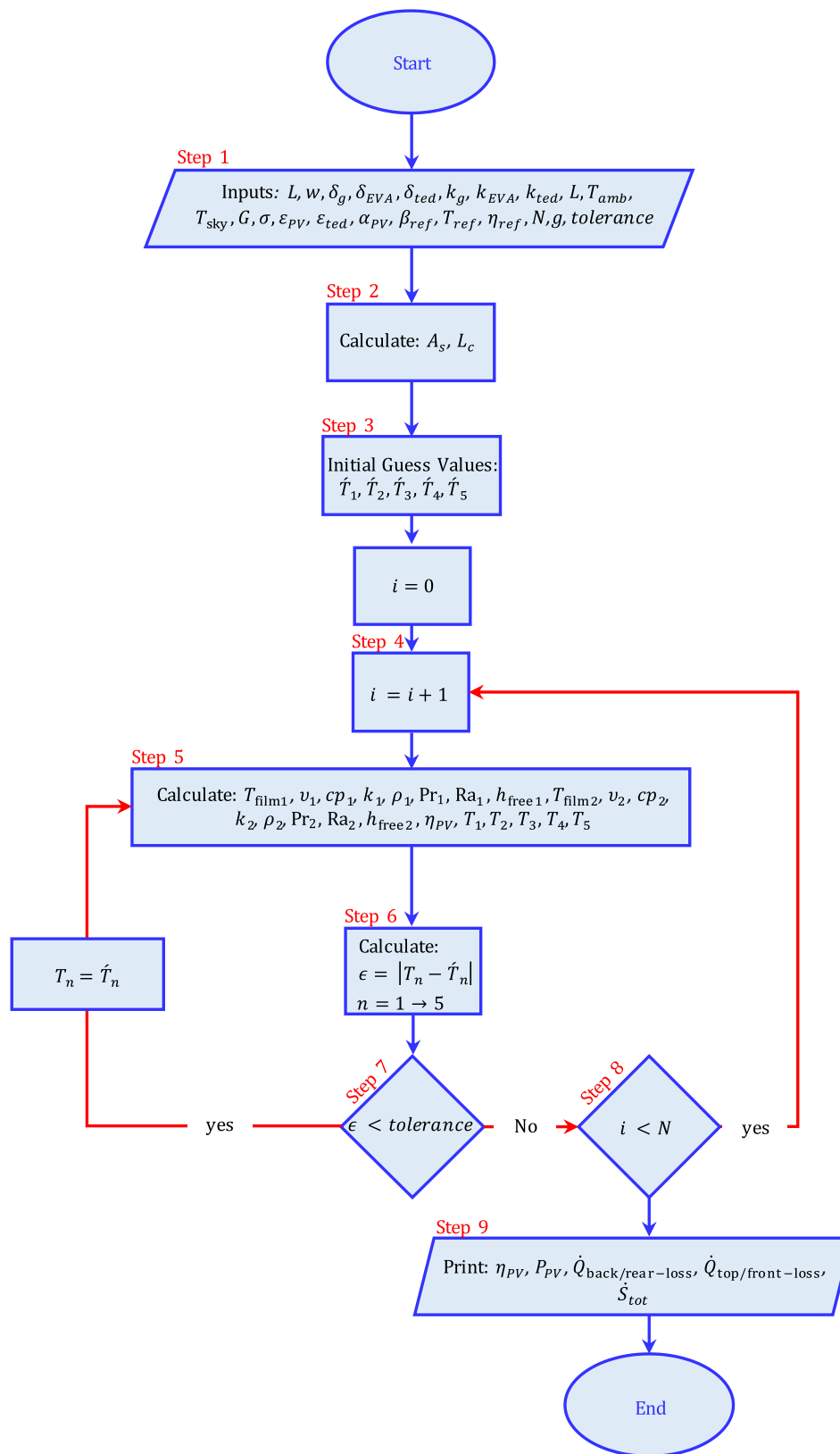
**Fig. A1**　Flow chart of the algorithm for the solution of the semi analytical model.

rear are predicted along with the electrical efficiency (η_{PV}). (SEE: Table B1.)

The energy balance equations are solved using fsolve to obtain new set of temperatures $(T_1, T_2, T_3, T_4, T_5)$ using Equations (13) and (14). The new values are compared with the old values which is based on the error value i.e. the difference between the old and new values to a tolerance of 1×10^{-4}. The program is executed repeatedly until all the various tem-peratures converge to the set tolerance. The collector temperatures are then used to calculate the useful PV electrical power by Equation (2) and the total incident radiation reaching the PV cell from Equation (11). The subscripts 1 and 2 refer to top/front or back/rear surfaces of PV module. N is the number of iteration and $\tilde{T}_n$ the guess value and T_n is the calculated value.

Appendix B. Meshing
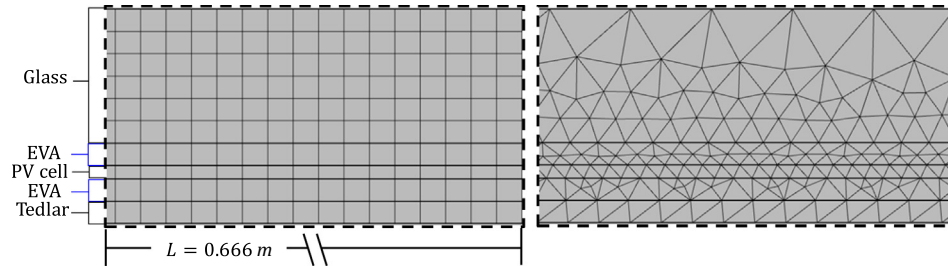
Fig. B1 Structured and unstructured mesh of standard PV unit for refinement step number (4) in Table B1.

Table B1 Grid independence test using structured and unstructured mesh element types for case study in Fallujah on a typical day in July under transient conditions.

Trial No	Refinement step	RAM (GB)	time (s)	NOE	MEQ	DOF	$T_{mpv}(°C)$
Unstructured mesh (triangular)							
1	extremely coarse	6.73	1357	15,765	0.345	34,834	48.23
2	very coarse	8.45	1867	21,121	0.343	45,954	48.31
3	less coarse	8.67	1819	20,176	0.357	44,163	48.30
4	Coarse	8.40	2020	22,188	0.356	48,249	48.32
Structured mesh (quadrilateral)							
1	extremely coarse	1.54	64	2142	1	10,011	48.32
2	very coarse	3.12	168	4242	1	19,409	48.20
3	less coarse	5.45	396	8127	1	36,141	48.22
4	Coarse	8.46	678	11,730	1	51,635	48.27

Appendix C. Module efficiency and PV power generation
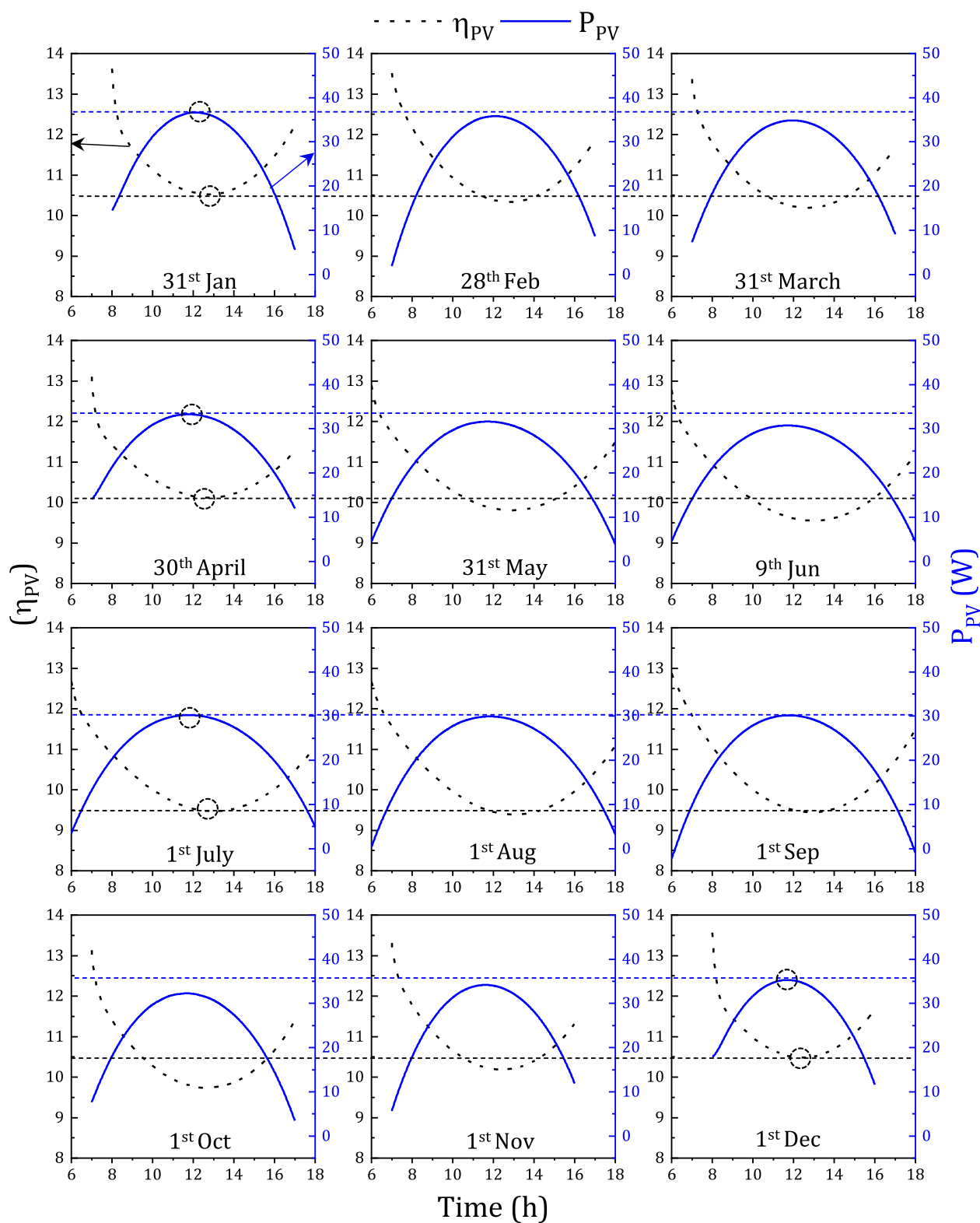
Fig. C1 PV module efficiency and power generation over a year in Fallujah city, using free convection and transient CFD model (time step is 1 min).

Table C1   Effect of length and tilt angle on the convective heat transfer coefficients of top and bottom surfaces of PV model in Fallujah on 31st January at 13:00.

Tilt angle	L/8	L/4	L/2	L	2L	4L	6L
$0(h_{\text{top}})$	7.52	6.6	5.89	5.76	5.773	5.78	5.783
$0(T_{mpv})$	54.25	56.13	57.72	58.33	58.59	58.75	58.80
$0(h_{\text{bottom}})$	3.75	3.29	2.93	2.672	2.502	2.4	2.363
$30(h_{\text{top}})$	5.17	4.35	3.67	3.1	4.505	4.471	4.316
$30(T_{mpv})$	55.47	58.00	60.27	62.01	57.59	58.00	58.18
$30(h_{\text{bottom}})$	5.14	4.32	3.65	3.08	4.471	4.34	4.283
$40(h_{\text{top}})$	5.47	4.59	3.89	3.286	4.505	4.471	4.316
$40(T_{mpv})$	54.72	56.90	59.52	61.32	57.59	58.00	58.18
$40(h_{\text{bottom}})$	5.43	4.56	3.86	3.265	4.471	4.34	4.283
$50(h_{\text{top}})$	5.68	4.78	4.04	3.43	4.505	4.471	4.316
$50(T_{mpv})$	54.18	56.69	58.66	61.16	57.59	58.00	58.18
$50(h_{\text{bottom}})$	5.46	4.478	4.015	3.41	4.471	4.34	4.283
$60(h_{\text{top}})$	5.84	4.91	4.15	3.53	4.505	4.471	4.316
$60(T_{mpv})$	53.88	56.18	58.29	60.80	57.59	58.00	58.18
$60(h_{\text{bottom}})$	5.79	4.88	4.13	3.505	4.471	4.34	4.283
$70(h_{\text{top}})$	5.94	5.01	4.23	3.592	4.505	4.471	4.316
$70(T_{mpv})$	53.53	56.08	58.04	60.56	57.59	58.00	58.18
$70(h_{\text{bottom}})$	5.9	4.97	4.205	3.572	4.471	4.34	4.283
$80(h_{\text{top}})$	6.00	5.06	4.277	3.632	4.505	4.471	4.316
$80(T_{mpv})$	53.47	55.93	57.90	60.42	57.59	58.00	58.18
$80(h_{\text{bottom}})$	5.96	5.03	4.25	3.61	4.471	4.34	4.283
$90(h_{\text{top}})$	6.02	5.07	4.298	3.64	4.505	4.471	4.316
$90(T_{mpv})$	53.34	55.74	58.18	60.06	57.59	58.00	58.18
$90(h_{\text{bottom}})$	5.98	5.04	4.27	3.616	4.471	4.34	4.283

REFERENCES

[1] A. PSE, Fraunhofer Institute For Solar Energy Systems ISE, Photovoltaics Report. (n.d.).

[2] A. Saxena, Varun, A.A. El-Sebaii, A thermodynamic review of solar air heaters, Renewable and Sustainable Energy Reviews. 43 (2015) 863–890. https://doi.org/10.1016/j.rser.2014.11.059.

[3] Adham Makki, Siddig Omer, Hisham Sabir, Advancements in hybrid photovoltaic systems for enhanced solar cells performance, Renewable and Sustainable Energy Reviews. 41 (2015) 658–684, https://doi.org/10.1016/j.rser.2014.08.069.

[4] Moustafa Al-Damook, Zain Alabdeen Hussein Obaid, Mansour Al Qubeissi, Darron Dixon-Hardy, Joshua Cottom, Peter J. Heggs, CFD modeling and performance evaluation of multipass solar air heaters, Numerical Heat Transfer, Part A: Applications. 76 (6) (2019) 438–464, https://doi.org/10.1080/10407782.2019.1637228.

[5] M.A. Green, Y. Hishikawa, E.D. Dunlop, D.H. Levi, J. Hohl-Ebinger, A.W. Ho-Baillie, Solar cell efficiency tables (version 52), Progress in Photovoltaics: Research and Applications. 26 (2018) 427–436, https://doi.org/10.1002/pip.3040.

[6] Y. Khalaf, O. Ibraheem, M. Adil, M. Salih, M. Qasim, K. Waleed, Maximum power point evaluation of photovoltaic modules under shading effect, European Scientific Journal. 10 (2014), https://doi.org/10.19044/esj.2014.v10n9p%25p.

[7] John K. Kaldellis, Marina Kapsali, Kosmas A. Kavadias, Temperature and wind speed impact on the efficiency of PV installations, Experience obtained from outdoor measurements in Greece, Renewable Energy. 66 (2014) 612–624.

[8] H.G. Teo, P.S. Lee, M.N.A. Hawlader, An active cooling system for photovoltaic modules, Applied Energy. 90 (1) (2012) 309–315, https://doi.org/10.1016/j.apenergy.2011.01.017.

[9] Hans J. Solheim, Hallvard G. Fjær, Einar A. Sørheim, Sean Erik Foss, Measurement and simulation of hot spots in solar cells, Energy Procedia. 38 (2013) 183–189, https://doi.org/10.1016/j.egypro.2013.07.266.

[10] Ya Brigitte Assoa, Luigi Mongibello, Anna Carr, Bernhard Kubicek, Maider Machado, Jens Merten, Siwanand Misara, Francesco Roca, Wendelin Sprenger, Martin Wagner, Shokufeh Zamini, Tomás Baenas, Philippe Malbranche, Thermal analysis of a BIPV system by various modelling approaches, Solar Energy. 155 (2017) 1289–1299, https://doi.org/10.1016/j.solener.2017.07.066.

[11] E. Skoplaki, J.A. Palyvos, Operating temperature of photovoltaic modules: A survey of pertinent correlations, Renewable Energy. 34 (1) (2009) 23–29, https://doi.org/10.1016/j.renene.2008.04.009.

[12] Shahzada Pamir Aly, Said Ahzi, Nicolas Barth, An adaptive modelling technique for parameters extraction of photovoltaic devices under varying sunlight and temperature conditions, Applied Energy. 236 (2019) 728–742, https://doi.org/10.1016/j.apenergy.2018.12.036.

[13] S. Zimmermann, H. Helmers, M.K. Tiwari, S. Paredes, B. Michel, M. Wiesenfarth, A.W. Bett, D. Poulikakos, A high-efficiency hybrid high-concentration photovoltaic system, International Journal of Heat and Mass Transfer. 89 (2015) 514–521, https://doi.org/10.1016/j.ijheatmasstransfer.2015.04.068.

[14] J.G. Ingersoll, Simplified Calculation of Solar Cell Temperatures in Terrestrial Photovoltaic Arrays, Journal of Solar Energy Engineering. 108 (1986) 95–101, https://doi.org/10.1115/1.3268087.

[15] D.L. King, Photovoltaic module and array performance characterization methods for all system operating conditions, in: AIP Conference Proceedings, American Institute of Physics, 1997, pp. 347–368. https://doi.org/10.1063/1.52852.

[16] M. Mattei, G. Notton, C. Cristofari, M. Muselli, P. Poggi, Calculation of the polycrystalline PV module temperature using a simple method of energy balance, Renewable Energy. 31 (4) (2006) 553–567, https://doi.org/10.1016/j.renene.2005.03.010.

[17] W.M. El-Maghlany, enass massoud, mohamed Elhelw, Novel Concept on the Enhancement of Conventional Solar Still Performance via Constant Heat Rate Supply to the Saline Water , In Review, 2021. https://doi.org/10.21203/rs.3.rs-224034/v1.

[18] J.A. Duffie, W.A. Beckman, Solar engineering of thermal processes /, 4th ed,., John Wiley, Hoboken, 2013.

[19] D.L. King, J.A. Kratochvil, W.E. Boyson, Photovoltaic array performance model, United States. Department of Energy, 2004.

[20] F. Lasnier, T.G. Ang, Photovoltaic Engineering Handbook, 1st ed., Routledge, 2017. https://doi.org/10.1201/9780203743393.

[21] S.A. Kalogirou, Y. Tripanagnostopoulos, Hybrid PV/T solar systems for domestic hot water and electricity production, Energy Conversion and Management 47 (2006) 3368–3382. https://doi.org/10.1016/j.enconman.2006.01.012.

[22] A.A. Farhan, A. Issam, M. Ali, H.E. Ahmed, Energetic and exergetic efficiency analysis of a v-corrugated solar air heater integrated with twisted tape inserts, Renewable Energy. 169 (2021) 1373–1385, https://doi.org/10.1016/j.renene.2021.01.109.

[23] R. Zhang, P.A. Mirzaei, J. Carmeliet, Prediction of the surface temperature of building-integrated photovoltaics: Development of a high accuracy correlation using computational fluid dynamics, Solar Energy. 147 (2017) 151–163, https://doi.org/10.1016/j.solener.2017.03.023.

[24] Mahmoud B. Elsheniti, Moataz A. Hemedah, M.M. Sorour, Wael M. El-Maghlany, Novel enhanced conduction model for predicting performance of a PV panel cooled by PCM, Energy Conversion and Management. 205 (2020) 112456, https://doi.org/10.1016/j.enconman.2019.112456.

[25] Arvind Tiwari, M.S. Sodha, Performance evaluation of solar PV/T system: an experimental validation, Solar Energy. 80 (7) (2006) 751–759, https://doi.org/10.1016/j.solener.2005.07.006.

[26] Karunesh Kant, A. Shukla, Atul Sharma, Pascal Henry Biwole, Thermal response of poly-crystalline silicon photovoltaic panels: Numerical simulation and experimental study, Solar Energy. 134 (2016) 147–155, https://doi.org/10.1016/j.solener.2016.05.002.

[27] Karunesh Kant, A. Shukla, Atul Sharma, Pascal Henry Biwole, Heat transfer studies of photovoltaic panel coupled with phase change material, Solar Energy. 140 (2016) 151–161, https://doi.org/10.1016/j.solener.2016.11.006.

[28] M. Al-Damook, Z. Khatir, M. Al Qubeissi, D. Dixon-Hardy, P.J. Heggs, Energy efficient double-pass photovoltaic/thermal air systems using a computational fluid dynamics multi-objective optimisation framework, Applied Thermal Engineering. 194 (2021) 117010, https://doi.org/10.1016/j.applthermaleng.2021.117010.

[29] Karima E. Amori, Mustafa Adil Abd-AlRaheem, Field study of various air based photovoltaic/thermal hybrid solar collectors, Renewable Energy. 63 (2014) 402–414, https://doi.org/10.1016/j.renene.2013.09.047.

[30] Yixian Lee, Andrew A.O. Tay, Finite element thermal analysis of a solar photovoltaic module, Energy Procedia. 15 (2012) 413–420, https://doi.org/10.1016/j.egypro.2012.02.050.

[31] F. Calise, R.D. Figaj, L. Vanoli, Experimental and numerical analyses of a flat plate photovoltaic/thermal solar collector, Energies. 10 (2017) 491, https://doi.org/10.3390/en10040491.

[32] M. Usama Siddiqui, A.F.M. Arif, Leah Kelley, Steven Dubowsky, Three-dimensional thermal modeling of a photovoltaic module under varying conditions, Solar Energy. 86 (9) (2012) 2620–2631, https://doi.org/10.1016/j.solener.2012.05.034.

[33] Y.A. Çengel, A.J. Ghajar, Heat and mass transfer: fundamentals & applications, Fifth edition., McGraw Hill Education, New York, NY, 2015.

[34] Stuart W. Churchill, Humbert H.S. Chu, Correlating equations for laminar and turbulent free convection from a vertical plate, International Journal of Heat and Mass Transfer. 18 (11) (1975) 1323–1329, https://doi.org/10.1016/0017-9310(75)90243-4.

[35] F.P. Incropera, A.S. Lavine, T.L. Bergman, D.P. DeWitt, Fundamentals of heat and mass transfer, Wiley, 2007.

[36] Z.R. Tahir, Muhammad Asim, Surface measured solar radiation data and solar energy resource assessment of Pakistan: A review, Renewable and Sustainable Energy Reviews. 81 (2018) 2839–2861, https://doi.org/10.1016/j.rser.2017.06.090.

[37] M. Al-Damook, Performance analysis of air-cooled photovoltaic/thermal systems, Ph.D., University of Leeds, 2019. http://etheses.whiterose.ac.uk/25298/ (accessed March 27, 2020).

[38] W.M. Kays, A.L. London, Compact heat exchangers, Repr. ed. 1998 with corrections, Krieger Pub. Co, Malabar, Fla, 1998.

[39] Mohamed A. Teamah, Ahmed F. Elsafty, Mahmoud Z. Elfeky, Enass Z. El-Gazzar, Numerical simulation of double-diffusive natural convective flow in an inclined rectangular enclosure in the presence of magnetic field and heat source, part A: Effect of Rayleigh number and inclination angle, Alexandria Engineering Journal. 50 (4) (2011) 269–282, https://doi.org/10.1016/j.aej.2010.05.001.

[40] Y.A. Cengel, A. Ghajar, Heat and mass transfer (a practical approach, SI version). 2011, McGraw-Hill Education, n.d.

[41] G.C. Vliet, Natural convection local heat transfer on constant-heat-flux inclined surfaces, Jounral of Heat Transfer 914 (1969) 511–516, https://doi.org/10.1115/1.3580235.

[42] Ali Radwan, Mahmoud Ahmed, The influence of microchannel heat sink configurations on the performance of low concentrator photovoltaic systems, Applied Energy. 206 (2017) 594–611, https://doi.org/10.1016/j.apenergy.2017.08.202.

[43] W.M. Deen, Analysis of transport phenomena, 2nd ed., Oxford University Press, New York, 2012.